ACS APPLIED ENERGY MATERIALS

www.acsaem.org Article

Fe_3O_4/ZrO_2 Composite as a Robust Chemical Looping Oxygen Carrier: A Kinetics Study on the Reduction Process

Qiming Tang, Yuxi Ma, and Kevin Huang*

Cite This: https://doi.org/10.1021/acsaem.1c01152 Read Online

ACCESS | Metrics & More | Article Recommendations | Supporting Information

ABSTRACT: FeO_x is the most popular choice of oxygen carriers for the chemical looping hydrogen (CLH) reactor and solid oxide iron−air redox battery (SOIARB) due to its earth abundance, low cost, and high oxygen content. However, the performance of an Fe/FeO_x chemical looping cycle is critically limited by the reduction kinetics of FeO_x. Aimed at understanding and ultimately improving the kinetics of FeO_x reduction, we here report a kinetics study on isothermal H_2 reduction of an Fe_3O_4/ZrO_2 composite (derived from Fe_2O_3/ZrO_2) and pure Fe_3O_4 (derived from Fe_2O_3) as an oxygen carrier in a CLH and SOIARB environment. We observe that the prevailing oxide form, on which the reduction kinetics is carried out, under 10% H_2O−Ar in 600−800 °C, is Fe_3O_4. We show that the reduction of Fe_3O_4 to Fe follows two consecutive steps and can be reasonably described by phenomenological chemical-controlled and diffusion-controlled kinetic models. We also demonstrate that the presence of ZrO_2 is critical in preventing Fe particles from sintering, obtaining reliable kinetic data, and stable operation of overall chemical looping cycles. The obtained kinetic parameters provide firsthand data for engineering and design of practical CLH reactors and SOIARBs.

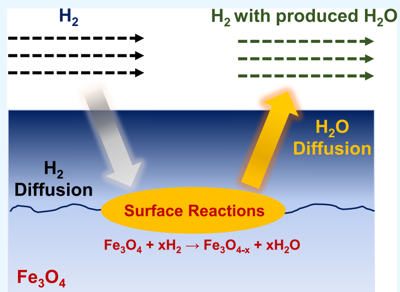

KEYWORDS: *Fe_3O_4, reduction kinetics, redox stability, chemical-control, diffusion-control*

■ INTRODUCTION

The increasing demand for more energy with a minimal impact on the environment has become a primary driver for current energy technology innovations. Hydrogen as an energy carrier has attracted significant interest in recent years from academic institutions and industries alike to substitute fossil fuels for a broad range of energy-related applications.[1−4] However, nearly 95% hydrogen is currently produced from steam methane reforming (SMR), a process emitting a significant amount of CO_2 (e.g., 9 kg CO_2/kg H_2 produced). The rest 5% H_2 is produced by water splitting technologies, which are more expensive than SMR (e.g., \$6/kg H_2 vs <\$2/kg H_2 for SMR). Chemical looping (CL) is a thermochemical process emerged in recent decades as a potential hydrogen production technology.[5−7] Collectively known as chemical looping hydrogen (CLH), the process undergoes consecutive oxidation and reduction cycles over a solid oxygen carrier (OC) such as oxides.[5] During the reduction cycle, a fuel (as a reducer) such as methane is oxidized, partially or fully depending on the application, by the lattice oxygen in an OC, producing reduced solid OC and oxidized gas-phase chemicals such as syngas. During the oxidation cycle, H_2O (as an oxidizer) is reduced to H_2, while the reduced solid OC is reoxidized. There are two basic types of CL reactor designs in the literature: moving bed and fixed bed, which are both under consideration for combined heat and chemical applications. Among all CL reactors, CLH is deemed a promising process to produce efficient and clean H_2. A successful integration of CLH technology into the current H_2 infrastructure will diversify H_2 production and energy storage for a clean energy economy.

CLH is also a key process inside a recently demonstrated solid oxide iron−air redox battery (SOIARB), which has a great potential for large-scale energy storage.[8−15] In this new battery system, a reversible solid oxide fuel cell (RSOFC) acts as an energy converter, while metal/metal oxide redox couples, such as Fe/Fe_2O_3, Mo/MoO_2, and W/WO_3, serve as an energy storage material (ESM). During the discharge cycle, H_2 produced from the H_2O-metal reaction in the ESM is electrochemically oxidized by O^{2-} to produce H_2O that migrates back to the ESM to sustain the H_2O-metal reaction. During the charging cycle, all the above reactions are reverse, while the RSOFC works as a water electrolyzer to produce H_2 for metal oxide reduction.

As a key element of CHL reactors and SOIARBs, OCs function as a medium to deliver pure O_2 without N_2 dilution to the fuel oxidation. There are a large body of OC materials reported in the literature, such as Fe_2O_3, NiO, CuO, Mn_2O_3 CeO_2, WO_3, etc.,[16−22] among which Fe-based OCs are the most used for CLH reactors and SOIARBs,[23,24] primarily due

Received: April 21, 2021
Accepted: June 21, 2021

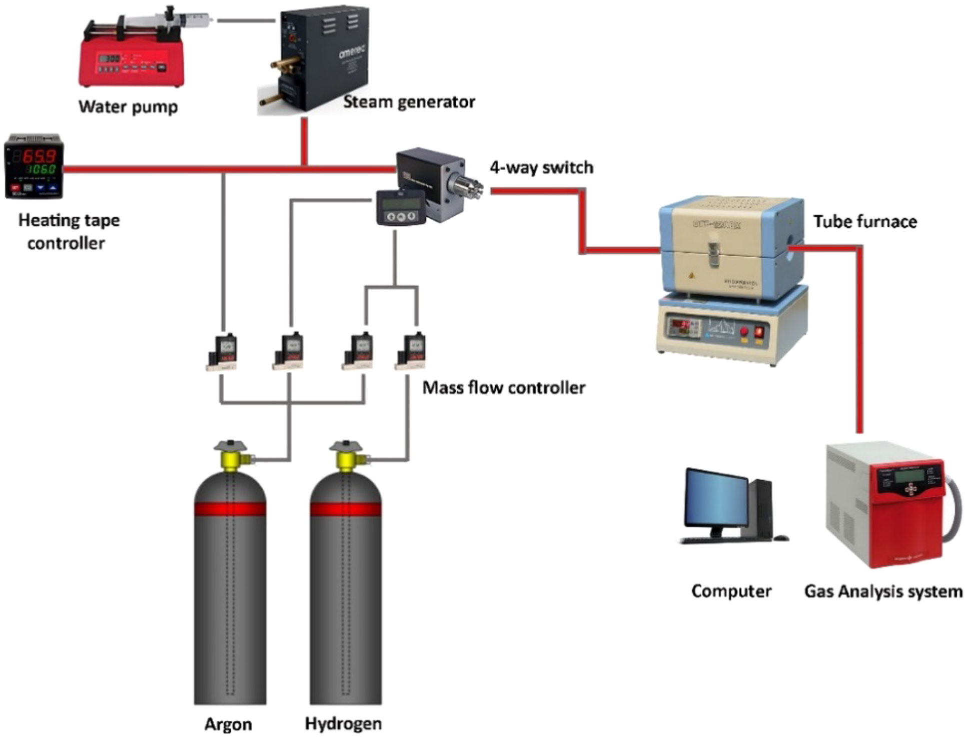

Figure 1. System setup for the kinetics study of FeO_x reduction.

to their earth abundance, low cost, environmental friendliness, high oxygen content, and relatively balanced thermodynamics and kinetics. However, one of the critical issues is the gradual sintering of Fe particles over repeated redox cycles, resulting in decreased kinetics and ultimately shortened service life. In practice, refractory materials such as ZrO_2, TiO_2, SiO_2, and Al_2O_3 are often added into Fe oxides to alleviate Fe sintering.[25−30] Among all sintering inhibitors studied, ZrO_2 stands out to be the most promising candidate due to its chemical inertness to Fe oxides and refractory nature.

Another pressing issue for Fe-based CLH and SOIARB is the need to have a clear understanding on the reduction mechanisms and obtain accurate kinetics data of Fe-based OCs mixed with sintering inhibitors. According to previous studies,[10,31] the reduction kinetics of FeO_x is a bottleneck to the overall performance of CLH and SOIARB. Indeed, there is a vast documentation on reduction kinetics studies of FeO_x in the literature.[32−36] However, they were mainly conducted on pure FeO_x, in which the rapid in situ sintering of the reduced Fe particles during the reduction process interferes an accurate evaluation of the data, thus resulting in inconsistent results in the literature. Since there is always a sintering inhibitor blended with the active Fe-based OCs in practical CLH reactors and SOIARBs, it will be more useful to appraise the true reduction kinetics of Fe oxides in the presence of a sintering inhibitor.

We here report an experimental evaluation and theoretical analysis of the reduction kinetics of an OC consisting of a starting Fe_2O_3/ZrO_2 composite in a CLH and SOIARB environment. Specifically, the kinetics of isothermal reduction of Fe_3O_4 (a reduced form of Fe_2O_3) with and without ZrO_2 has been studied using an online mass spectrometer, along with a phenomenological modeling analysis. The stability of the reduced form of the Fe_3O_4/ZrO_2 composite has also been assessed by performing redox (H_2/H_2O) cycles under a CLH-typical and SOIARB-typical environment.

EXPERIMENTAL METHODS

Materials Preparation. The starting Fe_2O_3/ZrO_2 composite OC was prepared by a co-precipitation method. Briefly, the stoichiometric solutions of $Fe(NO)_3{\cdot}9H_2O$ (≥99.999%, Sigma-Aldrich) and $ZrO(NO)_2{\cdot}6H_2O$ (≥99.999%, Alfa-Aesar) in mole ratios of Fe:Zr = 85:15 were first prepared by dissolving in deionized water. Then, these two solutions were mixed in a beaker with a cation concentration of 0.1 M, and polyvinylpyrrolidone (PVP, Sigma-Aldrich) as a surfactant was added while stirring constantly for 30 min. The resulting clear orange solution was then added dropwise to a slight excess of ammonium carbonate solution under constant stirring while the temperature of the solution was maintained at 35 °C. To ensure full precipitation of all the cations in the solution, the molar ratio of $(NH_4)_2CO_3$ (Sigma-Aldrich) and M^{n+} (M = Zr and Fe) was kept as $n(NH_4)_2CO_3{:}nM^{n+}$ = 2.5:1. The resulting brown precipitate was then left in the solution for 20 h with continuous stirring. Finally, the aged suspension precipitate was collected through a filter, washed several times with deionized water and ethanol by centrifugation, and finally dried overnight at 80 °C. To obtain the Fe_2O_3/ZrO_2 OC, the collected precipitate was calcined in static air at 600 °C for 2 h. Similarly, pure Fe_2O_3 OC was also synthesized with the same method but without $ZrO(NO)_2{\cdot}6H_2O$.

Materials Characterization. The phase compositions of the prepared Fe_2O_3/ZrO_2 and Fe_2O_3 OCs as well as the products of the redox reaction were examined by X-ray diffraction at a scan rate of 2° min^{-1} from 10 to 80° with a Rigaku D/MAX-2100. Their morphologies were also captured using a field emission scanning electron microscope (FESEM) (Zeiss Gemini500).

CLH Testing. *For Reduction Kinetic Data Collection.* To create a similar reaction environment to the CLH and SOIARB, reduction of the prepared Fe_2O_3/ZrO_2 and pure Fe_2O_3 OCs and their subsequent kinetics studies were performed in a fixed bed reactor; the experimental setup is illustrated in Figure 1.

The experimental system mainly consists of a quartz tube reactor, water pump, temperature controller, a program-controllable four-way

https://doi.org/10.1021/acsaem.1c01152
ACS Appl. Energy Mater. XXXX, XXX, XXX−XXX

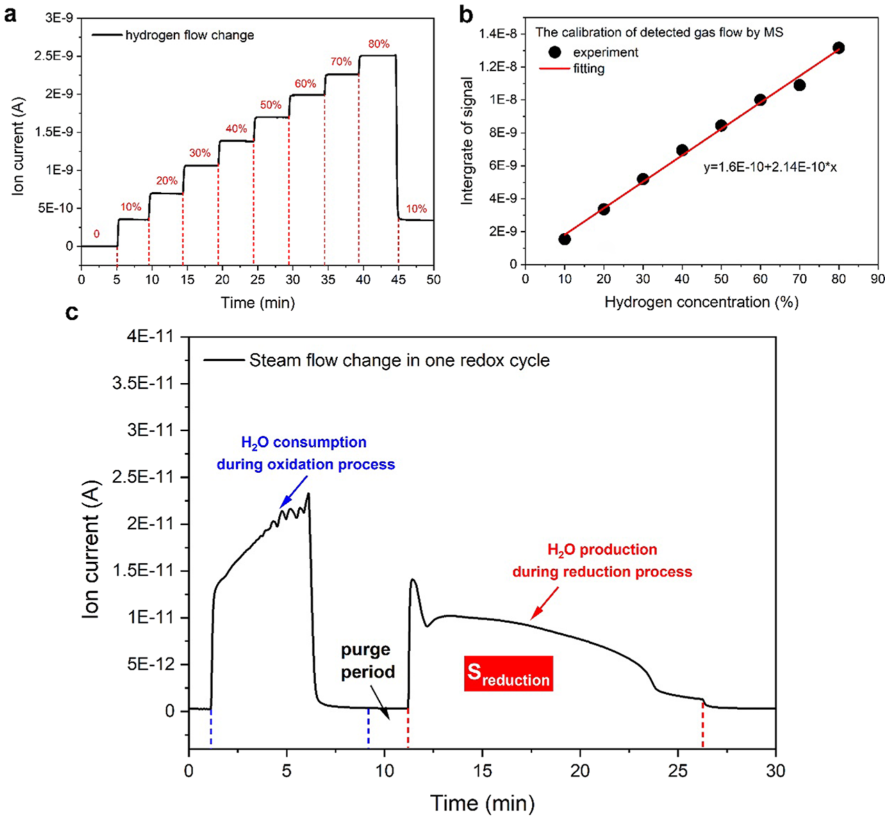

Figure 2. (a) Response of ion current in the MS system to the change of H_2 concentration. (b) Relationship between the integrated ion current and H_2 concentration. (c) Profile of change in outlet gas composition in one redox cycle between Fe_3O_4 and Fe.

switch, mass flow controllers, and a mass spectrometer (MS, Pfeiffer Omnistar 100) at the outlet of the reactor. The gas flow rate was controlled using a mass flow controller (Alicat Scientific MFC Series). The steam was generated from a homemade steamer operated at 120 °C with a DI water feed rate at 8.037 μL min^{-1} controlled using a syringe pump (SyringeONE Programmable syringe pump), which will produce 10 sccm H_2O. Approximately 100 mg of OC supported on a lump of quartz wool was placed inside a quartz glass tube, and then the furnace was heated to 400 °C under argon at 200 sccm. Then, a mixture of H_2 and Ar with different concentrations (5, 10, and 20% H_2) was introduced into the reactor during temperature ramp to the temperature of interest, i.e., 600, 650, 700, 750, and 800 °C. MS was performed to analyze the effluent compositions and confirm a full reduction of the starting Fe_2O_3 into Fe. At each temperature, it was held for 20 min before the first oxidation by H_2O and the following reduction by H_2. Note that under a CLH or SOIARB condition, the starting oxide composition for the reduction cycle depends on the temperature and partial pressure of oxygen (or the ratio of partial pressures of H_2O to H_2). Therefore, we have chosen to use a H_2O-oxidation cycle to create in situ the equilibrium Fe oxide composition for the subsequent reduction kinetics study. We will show later that this starting oxide composition for the reduction kinetics study is Fe_3O_4 under the experimental condition.

For Redox Cycle Long-Term Testing. In addition to the reduction kinetics study, we also performed a long-term redox cycle experiment on the starting Fe_2O_3/ZrO_2 and pure Fe_2O_3 OCs in the fixed bed reactor mentioned above. In a typical cycle, the sample at 700 °C was exposed to the following sequential atmospheres alternately achieved through a programable electric switch (Valco Instruments Co. Inc.): (i) 5 min of system purge with a flow of pure Ar (200 sccm), (ii) 5 min of oxidation under a flow of 10% H_2O in Ar (90 sccm), (iii) 5 min Ar purge (200 sccm), and (iv) 15 min reduction with 10% H_2 in Ar (90 sccm). The concentrations of Ar, H_2O, and H_2 in the effluent were continuously measured by an online MS system.

Data Processing. *MS Calibration.* To accurately determine the gas composition, we first performed calibration on an MS. The relationship between the ion current and the H_2 concentration read by MFC is shown in Figure 2a. As H_2 concentration increases, so does the ion current. Figure 2b shows the linear relationship between the H_2 concentration and the integrated ion current, from which the concentration of H_2 can be determined.

Reduction Kinetic Data. The reduction kinetics was evaluated by measuring the change in the H_2 or H_2O concentration in the effluent by MS. Figure 2c shows the ion−current change during one full redox cycle. The first peak corresponds to the outlet water signal during the H_2O oxidation process, and the second peak relates to the outlet water signal during the H_2 reduction process. The reduction extent, ξ (Fe_3O_4 to Fe), can be expressed as a function of time, t, using the following formula:

$$\xi(t) = \frac{\int_0^t (I_{H_2O\ pro})dt}{S_{red}} \tag{1}$$

Here, $I_{H_2O\ pro}$ is the time-dependent ion current related to H_2O production; S_{red} is the area of the reduction peak over the full reduction process.

Reduction Activity Retention. The reduction activity retention (AR) is defined in this study by the change of the integrated area of the outlet water signal, i.e.,

$$AR = \frac{S_{red,at\ nth\ cycle}}{S_{red.,max}} \times 100\% \tag{2}$$

where $S_{red,\ at\ nth\ cycle}$ is the integrated area of the outlet water signal at the nth cycle and $S_{red.\ ,\ max}$ is the maximal integrated area of the outlet water signal during the reduction cycle.

https://doi.org/10.1021/acsaem.1c01152
ACS Appl. Energy Mater. XXXX, XXX, XXX−XXX

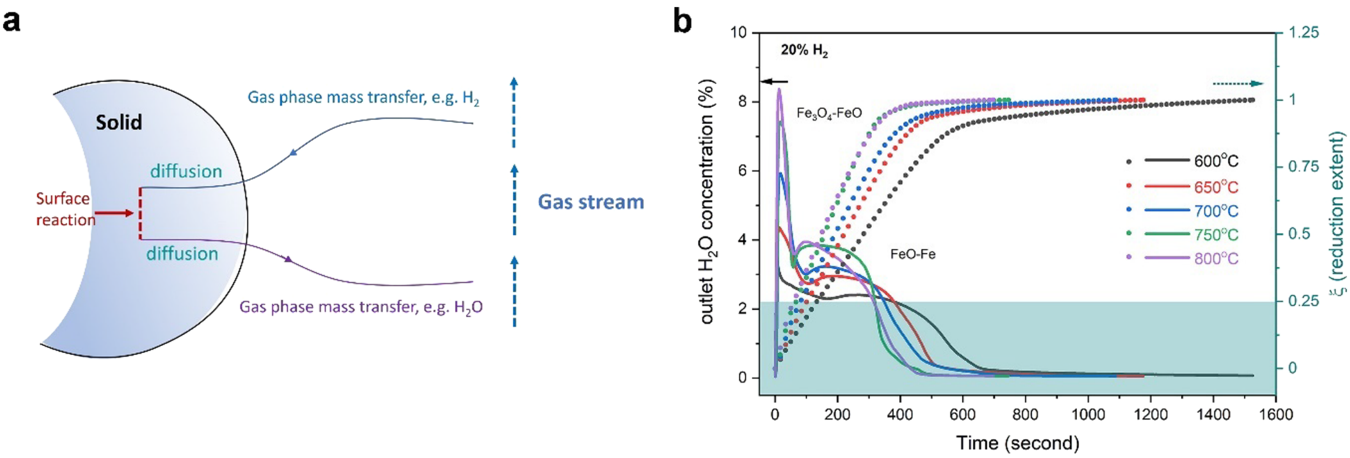

Figure 3. (a) Schematic diagram of the reaction between a gas and solid particle. (b) Outlet H_2O concentration and reduction extent of Fe_3O_4 vs time with an inlet 20% H_2. Dots: reduction extent; lines: H_2O concentration measured by MS.

RESULTS AND DISCUSSION

Phenomenological Models for Fe Oxide Reduction. Generally, the reduction of iron oxides by H_2 is a complex, heterogeneous gas–solid reaction.[36] A schematic representation of the reaction between gas and solid particles is illustrated in Figure 3a. During the reduction, a gaseous reactant, such as H_2, will first reach the external surface of the solid material and enter the internal body of the solid through pores. The reactant will then adsorb on the surface of the solid, where a chemical reaction takes place, forming gaseous products and new phases on the solid surface. Finally, the gaseous products diffuse out of the porous solid body and entrain into the bulk gas phase. Therefore, the kinetics of a gas–solid reaction could be limited by the rates of the diffusion process and surface reaction, whichever is slower. If a dense outer shell forms during the reaction or if agglomeration occurs, the progress of the reaction can become limited by the diffusion process. In this case, both chemical and diffusion kinetics must be considered.

The following generic phenomenological kinetic equations have been used to represent the kinetics of reduction

$$\frac{d\xi}{\mathrm{d}t} = kf(\xi) \tag{3}$$

where $\frac{d\xi}{\mathrm{d}t}$ represents the kinetic rate; t is the reduction time; ξ is the reduction extent; k is the rate constant, which is expressed by $k = A\exp\left(-\frac{E_a}{RT}\right)$, where A, E_a, R, and T are the pre-exponential factor, activation energy, gas constant, and temperature, respectively; and $f(\xi)$ is a mathematical function that depends on the controlling mechanisms. If the reaction is controlled by a chemical reaction, $f(\xi) = 3(1-\xi)^{2/3}$; if it is limited by the diffusion in the product layer, $f(\xi) = 3/2(1-\xi)^{2/3} \times (1-(1-\xi)^{1/3})$.[33]

For reaction kinetics under isothermal conditions, the rate of eq 3 can be analytically integrated to yield

$$g(\xi) = \int_0^{\xi} \frac{d\xi}{f(\xi)} = kt \tag{4}$$

where $g(\xi)$ is an integral mathematical function related to mechanisms of the reduction reaction.

Therefore, the relationship between the extent of reduction and time can be obtained, from which the kinetic rate constant k can be further determined.

For reduction that is chemical reaction controlled,

$$\xi = 1 - (1-kt)^3 \tag{5}$$

For reduction that is controlled by diffusion in the product layer,

$$\xi = 1 - (1-\sqrt{kt})^3 \tag{6}$$

Determination of a Stable Fe Oxide Phase for a Reduction Study. The reduction kinetic behavior of Fe oxides in H_2 has been investigated extensively by a thermogravimetric (TG) method. However, there are fewer reports in the literature on using the MS method. Through analyzing the outlet gas compositions, the phenomenologically based mechanisms of reactions can be analyzed with accuracy and high fidelity. Figure 3b shows variations of the outlet H_2O concentration during a live reduction of Fe_3O_4 (after a full reduction from Fe_2O_3 to Fe in the starting Fe_2O_3/ZrO_2 and subsequent oxidation to Fe_3O_4 in 10% H_2O) and the corresponding reduction extent vs time at different temperatures (600–800 °C) in 10% H_2–Ar. The reduction extent was calculated from eq 1. The outlet H_2O concentration measured by MS increases rapidly at the beginning of the reaction, reaching a temporal maximum and then decreases toward the end of reduction, suggesting that the reduction is initially fast and then becomes slow. Also as expected, the rate of reduction is significantly faster at higher temperatures than at lower temperatures. The two peaks shown in Figure 3b appears to suggest that there are two distinct reactions involved in the reduction, which are related to the following reactions:

$$Fe_3O_4 + H_2 \rightarrow 3FeO + H_2O \tag{7}$$

$$3FeO + 3H_2 \rightarrow 3Fe + 3H_2O \tag{8}$$

For the initial sharp peak, corresponding to $\xi = 0$–0.25, it suggests that it is related to the reduction of Fe_3O_4 to FeO based on the 1:3 H_2 stoichiometry between reactions 7 and 8, while the second broader peak corresponding to a larger $\xi = 0.75$ is related to the reduction of FeO to Fe. It is worth noting that the rate of reduction slows down with time, especially after a reduction extent of 0.9, which is likely related to the low

https://doi.org/10.1021/acsaem.1c01152
ACS Appl. Energy Mater. XXXX, XXX, XXX−XXX

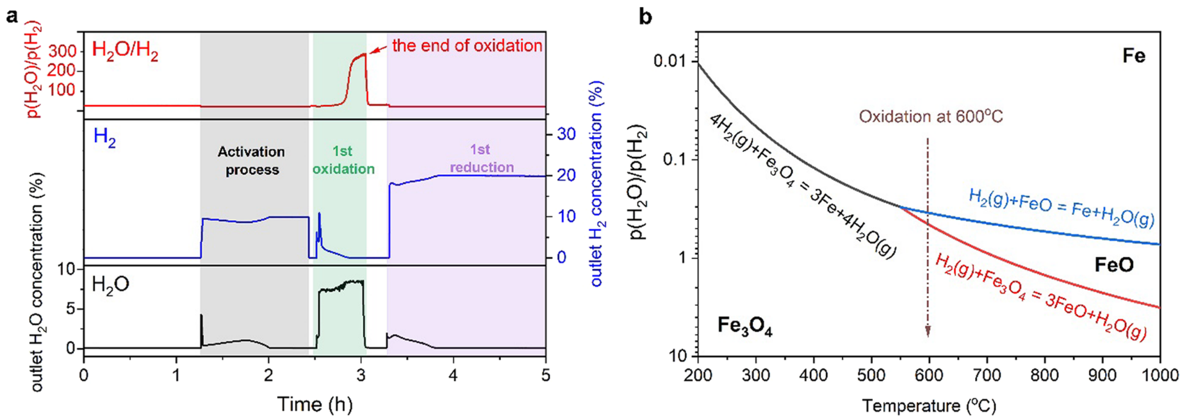

Figure 4. (a) Outlet H_2O and H_2 concentrations and the corresponding $p(H_2O)/p(H_2)$ vs time during oxidation at 600 °C. (b) Thermodynamic phase stability diagram of an Fe−O−H system. This plot is constructed by HSC Chemistry 5.0

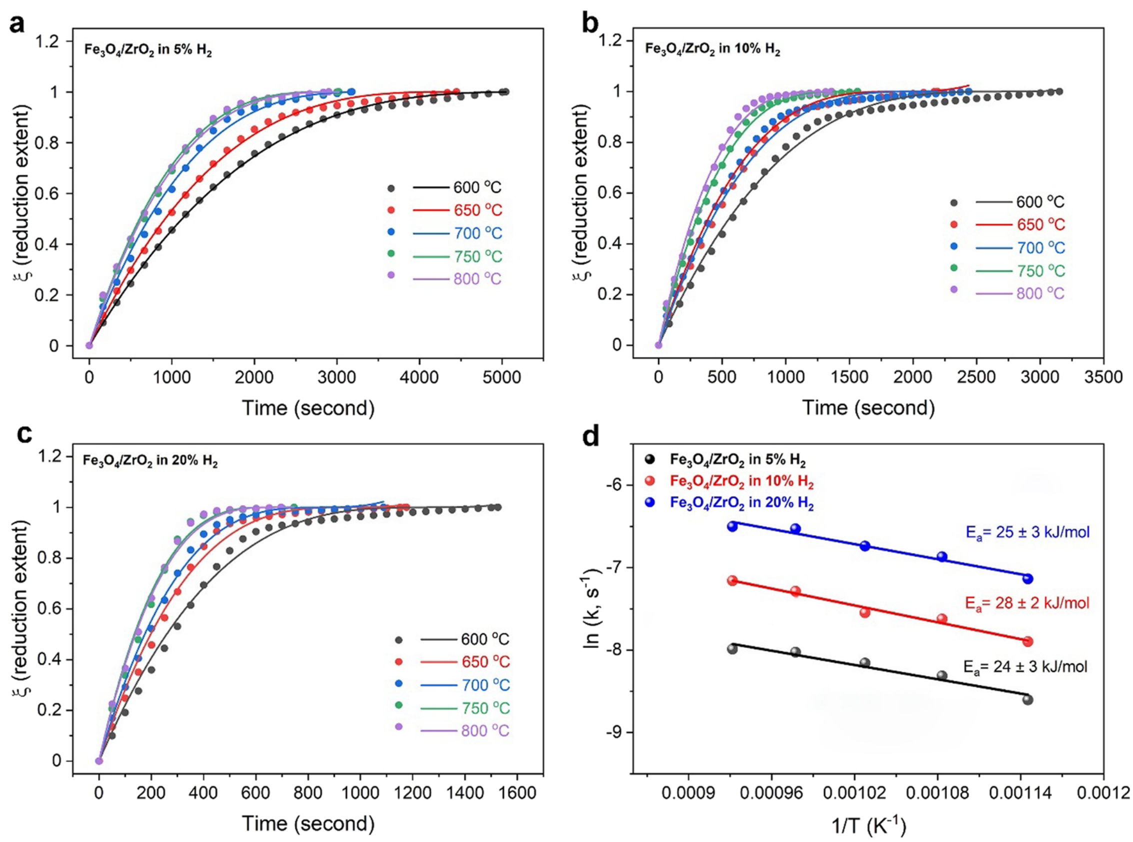

Figure 5. Reduction extent of Fe_3O_4 vs time at 600 to 800 °C in (a) 5% H_2, (b) 10% H_2, and (c) 20% H_2. (d) Arrhenius plots of the reduction rate constant of Fe_3O_4 at different H_2 contents based on the chemical-controlled model.

fraction of FeO and impeded diffusion by partial Fe particle sintering. We will discuss the latter in a later section.

To confirm the final FeO_x composition after oxidizing Fe by 20% H_2O (note: Fe was derived from an initial full reduction of Fe_2O_3/ZrO_2 in pure H_2), the ratio of partial pressures of H_2O and H_2 that are in equilibrium with the formed Fe oxide was calculated based on the outlet H_2O and H_2 concentrations measured by MS. The raw experimental results are shown in Figure 4a, along with Figure 4b that shows the calculated thermodynamic phase stability diagram of an Fe−O−H system. It is evident that at all experimental temperatures above 600 °C and pH_2O/pH_2 ~220, Fe_3O_4 will be the stable oxide phase. Therefore, it is the starting oxide for our H_2-reduction kinetics study.

Modeling of Experimental Data. Figure 5a−c shows the grouped isotherms of the normalized Fe_3O_4 reduction extent vs time from 600 to 800 °C in different inlet H_2 concentrations. It is seen that all curves exhibit a rapid increase in the early stage of reduction followed by a slower increase to the final plateau. As expected, the rate of conversion from Fe_3O_4 to Fe increases with the reaction temperature and H_2 content. We here use the chemical reaction-controlled model discussed above to fit the data, from which the rate constant (k) vs T are obtained. Figure 5d shows the Arrhenius plots of k, from which the activation energies (E_a) are found to

https://doi.org/10.1021/acsaem.1c01152
ACS Appl. Energy Mater. XXXX, XXX, XXX−XXX

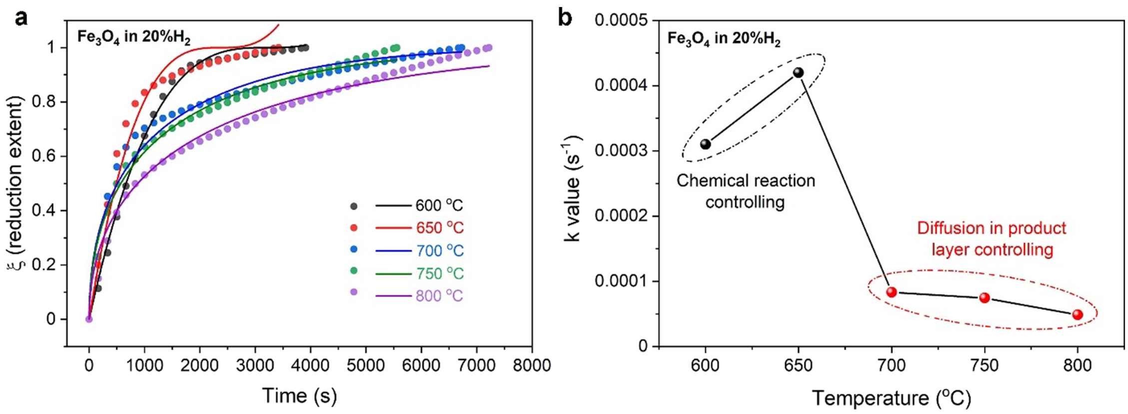

Figure 6. (a) Reduction extent of Fe_3O_4 derived from a pure Fe_2O_3 vs time at 600 to 800 °C in 20% H_2. (b) Rate constant of reduction of Fe_2O_3-derived Fe_3O_4 at different temperatures in 20% H_2.

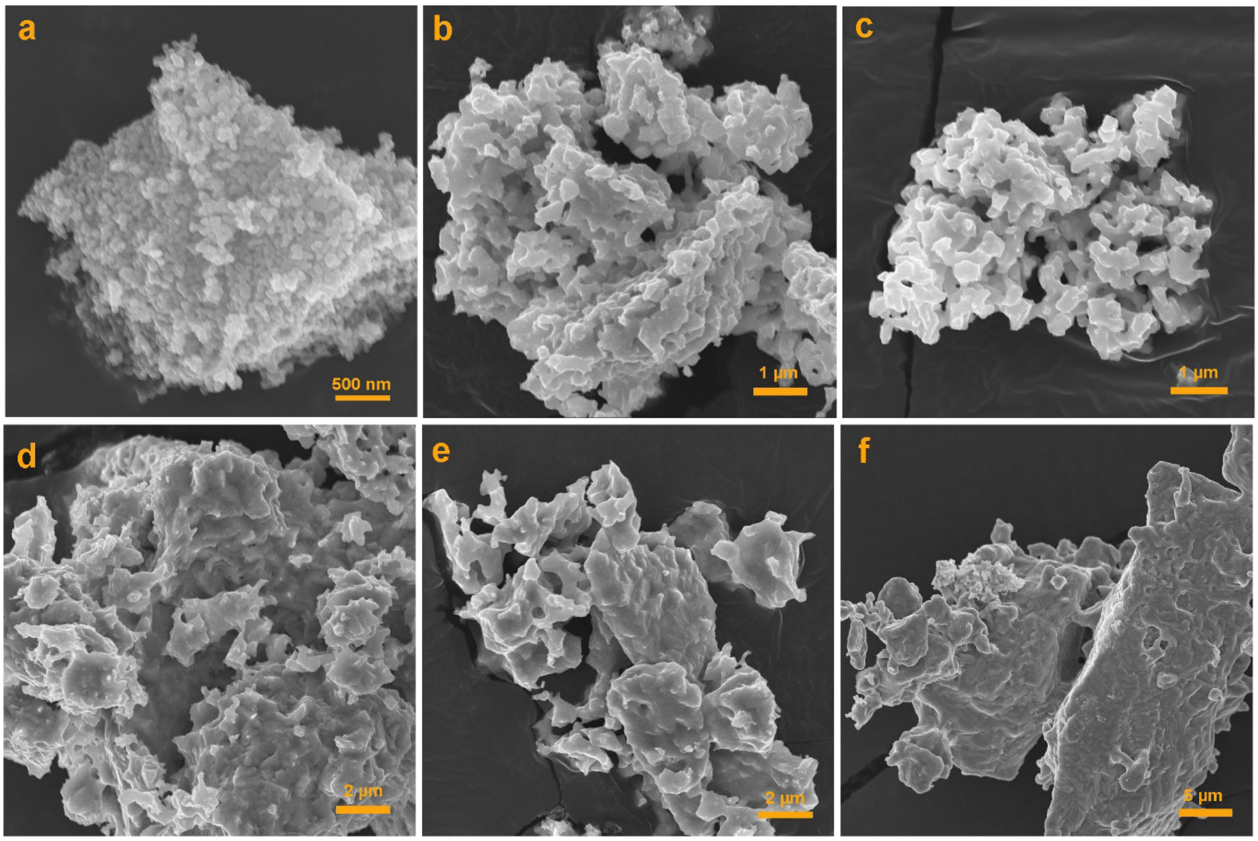

Figure 7. SEM images of (a) pure Fe_2O_3 before testing and after testing in 20% H_2 at (b) 600, (c) 650, (d) 700, (e) 750, and (f) 800 °C.

be 24 ± 3, 28 ± 2, and 25 ± 3 kJ/mol for 5, 10, and 20% H_2, respectively. These activation energies fall within the range of the reported values,[32] but it seems that E_a is less sensitive to the H_2 content. The actual values of k and E_a along with the fitting reliability are summarized in Table S1 for reference.

Figure 6a shows the reduction degree of pure Fe_3O_4 (derived from a pure Fe_2O_3) vs time obtained at different temperatures and fixed inlet 20% H_2. Note that we here only show the results in 20%H_2 but expect the same trend in 5 and 10% H_2. Compared to the data derived from the Fe_2O_3/ZrO_2 composite, the results clearly indicate a different reduction behavior. When the temperature is above 650 °C, instead of increasing with temperature, the rate of reduction in fact gradually decreases. This could be explained by the sintering of Fe particles, forming a dense layer limiting mass transfer (see the morphology later). Therefore, different from Fe_3O_4 derived from Fe_2O_3/ZrO_2, a diffusion-controlled model should be also considered for the case of pure Fe_3O_4 reduction above 700 °C. The results of both chemical-controlled (600 and 650 °C) and combined chemical-controlled and diffusion-controlled model (700−800 °C) are shown in Figure 6b. Clearly, the merits-of-figure of fittings are not as good as Fe_3O_4/ZrO_2 of Figure 6a. Fe particle sintering, which was not considered in the modeling, is deemed as the reason for the poorer fitting. Nevertheless, the rate constants derived from the chemical-controlled model increase with temperature until particle agglomerations prevail above 650 °C. Since the dense product layer formed during the reduction process prevents the inward

https://doi.org/10.1021/acsaem.1c01152
ACS Appl. Energy Mater. XXXX, XXX, XXX−XXX

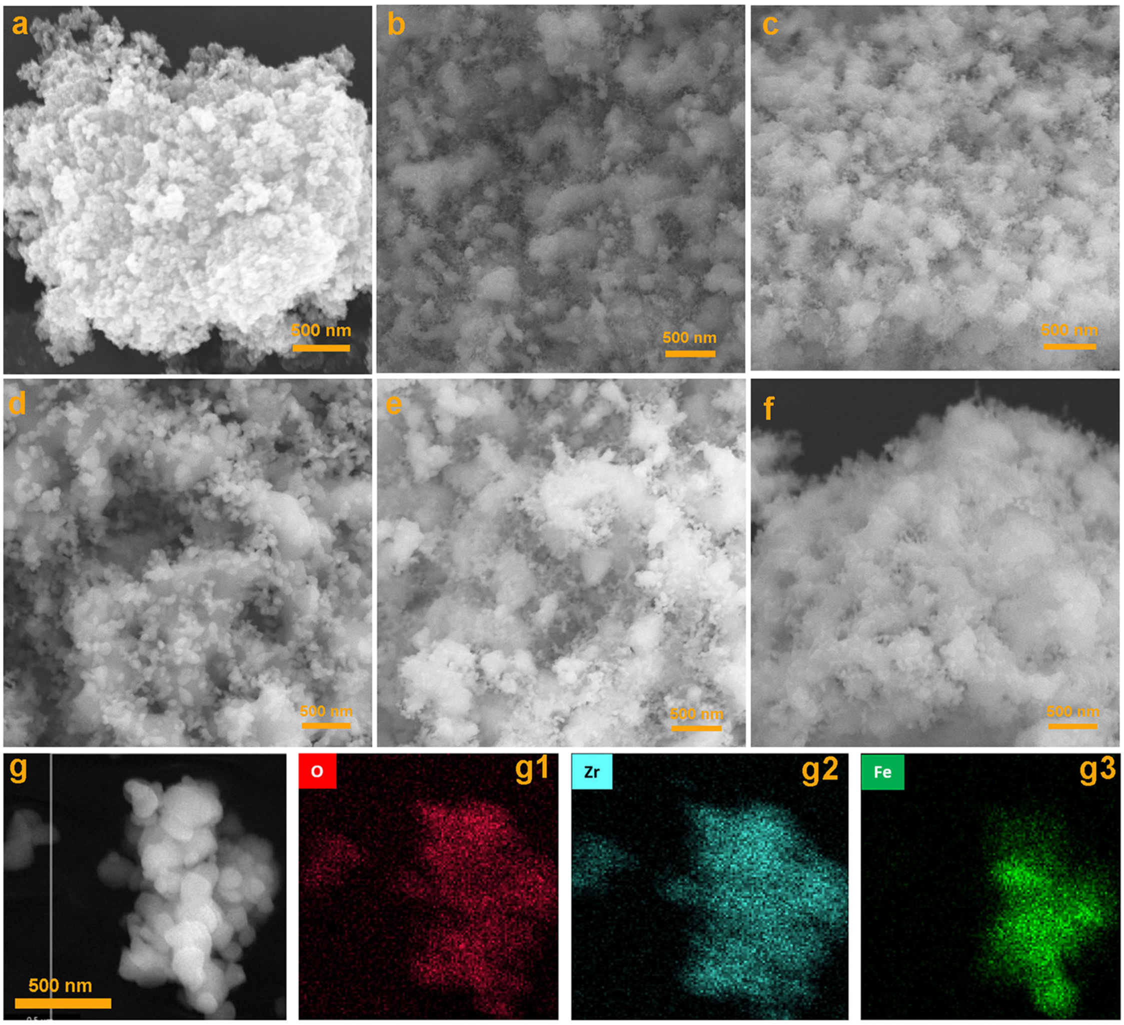

Figure 8. (a) SEM images of Fe_2O_3/ZrO_2 before reduction; after reduction in 20% H_2 at (b) 600, (c) 650, (d) 700, (e) 750, and (f) 800 °C; (g) elemental mapping of O, Zr, and Fe after reduction.

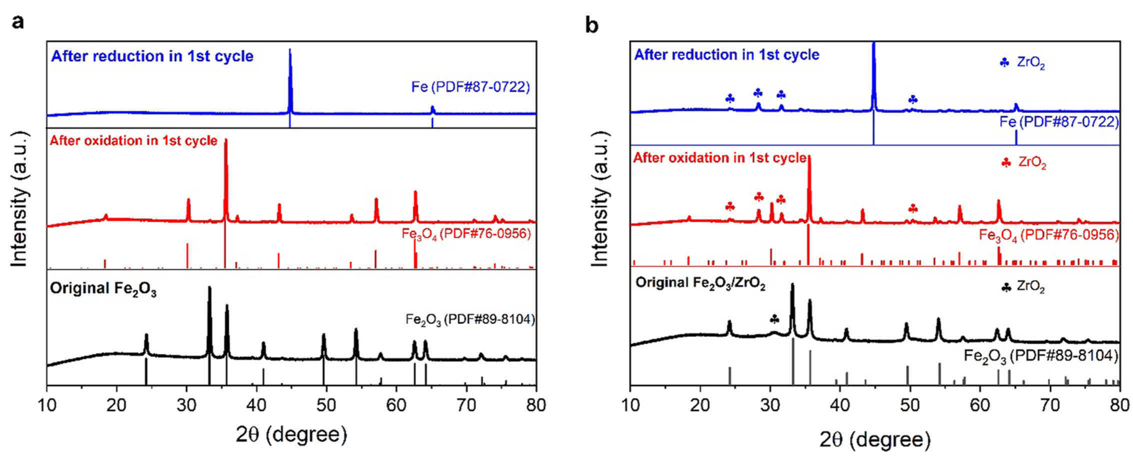

Figure 9. Comparison of XRD patterns of the as-prepared precursors of Fe_2O_3 (a) and Fe_2O_3/ZrO_2 (b) before and after the first oxidation in 10% H_2O and reduction in 20% H_2 at 700 °C.

and outward diffusions of H_2 and H_2O, respectively, a further reduction will likely be controlled by the diffusion beyond this point. Furthermore, with the increase in temperature, the sintering effect becomes more pronounced, resulting in a lowered rate constant instead. The kinetic parameters obtained are summarized in Table S2, which shows a generally lower rate constant than that derived from Fe_2O_3/ZrO_2. Therefore, the inert ZrO_2 additive plays a beneficial role in retaining the high reduction kinetics of Fe_3O_4.

Morphologies of Fe Oxide Before and After Reduction. The SEM images of the original pure Fe_2O_3 and post-tested one at different temperatures in 20% H_2 are shown in

https://doi.org/10.1021/acsaem.1c01152
ACS Appl. Energy Mater. XXXX, XXX, XXX−XXX

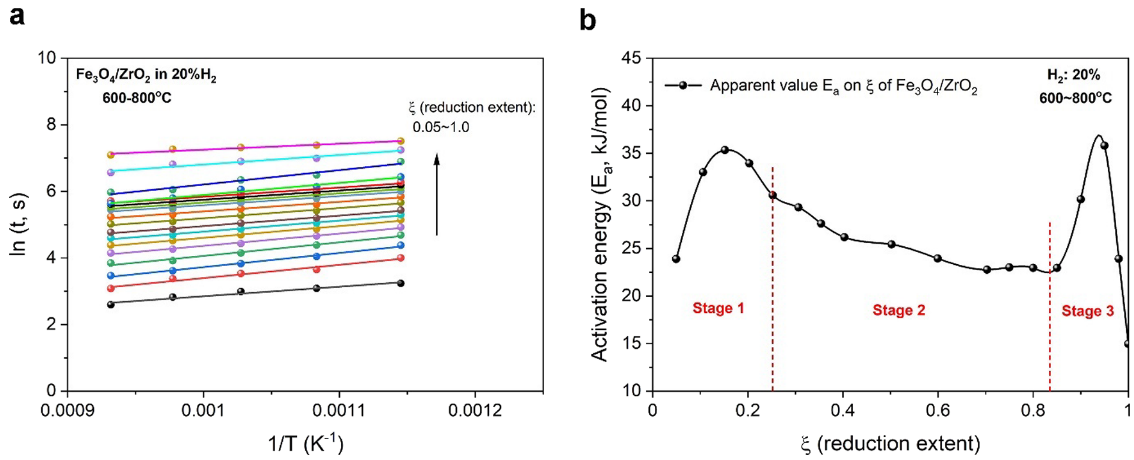

Figure 10. (a) Plots of ln t vs $1/T$ at different reduction extents and temperatures of 600−800 °C in 20% H_2. (b) Activation energy as a function of the reduction extent (ξ).

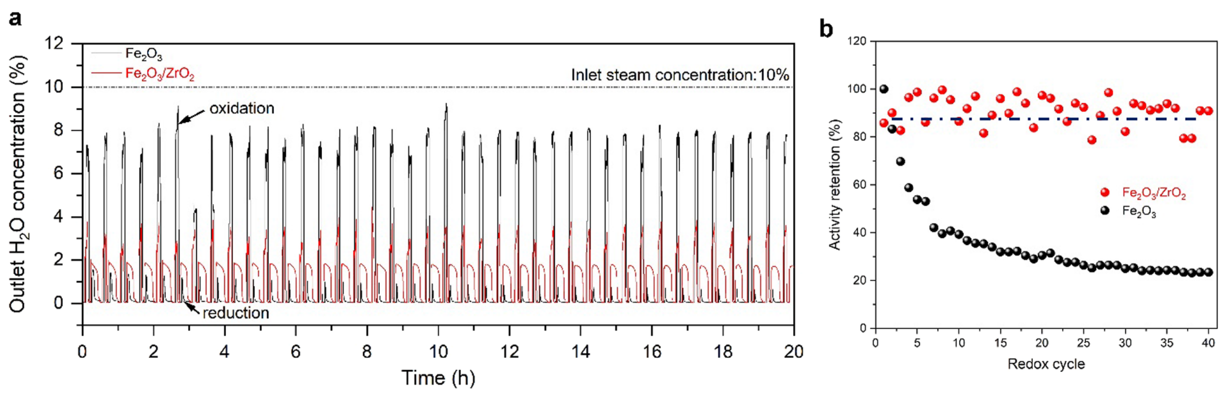

Figure 11. (a) Profile of H_2O concentrations during redox cycling with Fe_2O_3/ZrO_2 and Fe_2O_3 as the OC. (b) Redox activity retention of Fe_2O_3/ZrO_2 and Fe_2O_3.

Figure 7, where a significant morphological change with temperature is observed. Figure 7a depicts the morphology of the original Fe_2O_3 powders prepared through co-precipitation and calcination at 600 °C for 5 h. Nanoscaled Fe_2O_3 particles are clearly seen to evenly distribute within soft agglomerates. After the reduction study at 600 °C, Figure 7b shows a partial shrinkage with a small degree of agglomeration and some porosity. As the temperature increases from 600 to 800 °C, Figure 7c−f shows that the surface of the sample exhibits severe agglomeration and becomes denser. A denser microstructure is evidently observed when the reduction temperature is above 650 °C, which is a direct evidence for the blocked diffusion and lowered kinetic rate.

In contrast, samples derived from Fe_2O_3/ZrO_2 have a different morphology after a similar reduction process. Figure 8a shows the morphology of the Fe_2O_3/ZrO_2 powder before testing. It exhibits uniform nanoparticles like pure Fe_2O_3. After testing, Figure 8b−f shows that it still retains a nanoscaled morphology. The element mapping in Figure 8g confirms the homogeneous distributions of Fe and Zr even in the reduced powder.

Phase Compositions of Fe Oxides. The phase compositions revealed by the XRD of the pure Fe_2O_3 and Fe_2O_3/ZrO_2 composite OCs before and after the first redox cycle are shown in Figure 9. Both as-prepared pure and Fe_2O_3/ZrO_2 composite consist of the expected phases. For the pure Fe_2O_3 precursor, Figure 9a shows that the Fe oxidation product by 10% H_2O is magnetite (Fe_3O_4) instead of hematite (Fe_2O_3) or wüstite (FeO) at 700 °C, consistent with the thermodynamic prediction (see Figure 4b). In the following reduction process, Fe_3O_4 is fully reduced to Fe. Thus, Fe/Fe_3O_4 is the active redox couple for CLH under this condition. Figure 9b shows similar phase compositions for Fe_2O_3/ZrO_2 after the first redox cycle. During the redox process, all XRD peaks of ZrO_2 remain unchanged, even though the peak at 28.2° is weak due to the high crystallinity and high content of Fe_2O_3, suggesting its chemical stability to Fe-based materials and H_2.

An Analytical Approach. To further provide a clearer picture of the phenomenological mechanisms of reduction of Fe_3O_4 derived from Fe_2O_3/ZrO_2, a model-free analytical approach was also adopted.[33,37] From eq 4, it can be rearranged into

$$\ln(t) = (-\ln A + \ln(g(\xi))) + E_a/RT \tag{9}$$

By plotting ln t versus $1/T$, the activation energies can be obtained at any reduction extents from the slope of a fitting line. Figure 10a shows the fittings at $\xi = 0.05$ to full reduction at 600−800 °C in 20% H_2, while Figure 10b shows the derived E_a vs ξ. According to a previous report,[33] the process of reduction can be described by single-step kinetics if E_a does not vary with ξ. In this case, with increasing ξ, E_a first increases from 24 to 35 kJ/mol within $0.05 < \xi < 0.15$, then decreases to 22 kJ/mol within $0.15 < \xi < 0.85$, and then increases to 37 kJ/

https://doi.org/10.1021/acsaem.1c01152
ACS Appl. Energy Mater. XXXX, XXX, XXX−XXX

mol within $0.85 < \xi < 0.95$, and finally decreases to 15 kJ/mol at the end of reduction. These variations reflect the changes in nucleation and growth mechanisms during the reduction process. Combined with the kinetic data and XRD results, we divide the reduction process into three steps: (1) the first stage is attributed to the reduction of Fe_3O_4 to FeO ($0 < \xi < 0.25$); its high E_a implies that it might be a limiting step; (2) the second stage is a further reduction from FeO to Fe ($0.25 < \xi < 0.85$), during which E_a decreases with the reduction process; and (3) the last stage is related to a diffusion process, during which the reduction rate slows down, as shown in Figure 5c, with an increased E_a. In addition, at the end of a reduction period, the gradually densified Fe outer layer also presents a barrier to the reduction, resulting in a higher E_a.

Redox Stability in a CLH Reactor. The stability of redox activity of the Fe_3O_4/ZrO_2 OC was also tested in a chemical looping system with an on-line MS. Figure 11a shows a profile of H_2O concentration variations over 40 redox cycles. The sharp higher and lower peaks are produced from the process of oxidation and reduction, respectively. The redox activity is obtained by the area of the water peak according to eq 2. Figure 11b shows activity retention (AR) vs cycle number of Fe_3O_4/ZrO_2 OC, demonstrating 90% AR after 40 cycles at 700 °C with 10%H_2−Ar and 10%H_2O−Ar as the reduction and oxidation gases, respectively. In comparison, pure Fe_3O_4 OC shows a rapid decay with a redox cycle, retaining only 20% activity after 40 cycles. Compared to other OCs,[38,39] these results further confirm that ZrO_2 is an important component to achieve stable redox cycles for Fe-based OC materials. We acknowledge that while Fe_3O_4/ZrO_2 exhibits much better stability than pure Fe_3O_4, its practicality in CLH applications still needs further development to overcome "Kirkendall diffusion"-induced gradual separation of Fe and ZrO_2.[40] A mitigation approach is to alloy Fe with Ni to prevent the Kirkendall effect.[41]

■ CONCLUSIONS

The H_2 reduction kinetics of Fe_3O_4 derived from Fe_2O_3/ZrO_2 and pure Fe_2O_3 have been investigated by MS in a temperature range of 600−800 °C and H_2 content of 10−20%. The reduction in Fe_3O_4/ZrO_2 can be described as a multistep reaction, which can be modeled by a chemical-controlled model. For pure Fe_3O_4, however, the reduction kinetics can only be described by a chemical-controlled model in 600−650 °C, but it must be described by a combined chemical-controlled and diffusion-controlled model above 700 °C due to its serious sintering effect. The redox cycle stability testing indicates that Fe_3O_4/ZrO_2 is a much more stable OC than pure Fe_3O_4. Overall, this work demonstrates the need for ZrO_2 to achieve stable performance and provides key kinetic data for engineering design of practical CLH reactors and SOIARB systems in the future. However, we acknowledge that while adding ZrO_2 to the Fe-oxide OC bed would enhance the stability, it also reduces H_2 producing capacity. Future development of suitable Fe alloys could solve the activity and stability at once.

■ ASSOCIATED CONTENT

Supporting Information

The Supporting Information is available free of charge at https://pubs.acs.org/doi/10.1021/acsaem.1c01152.

Tables for summaries of rate constants and activation energies (Tables S1 and S2) (PDF)

■ AUTHOR INFORMATION

Corresponding Author

Kevin Huang − *Department of Mechanical Engineering, University of South Carolina, Columbia, South Carolina 29201, United States*; orcid.org/0000-0002-1232-4593; Email: huang46@cec.sc.edu

Authors

Qiming Tang − *Department of Mechanical Engineering, University of South Carolina, Columbia, South Carolina 29201, United States*

Yuxi Ma − *Department of Mechanical Engineering, University of South Carolina, Columbia, South Carolina 29201, United States*

Complete contact information is available at: https://pubs.acs.org/10.1021/acsaem.1c01152

Author Contributions

Q.T. carried out the experiments and data processing. Y.M. carried out the analysis principle and explanation of results. K.H. carried out the explanation of results. The manuscript was written through contributions of all authors. All authors have given approval to the final version of the manuscript.

Notes

The authors declare no competing financial interest.

■ ACKNOWLEDGMENTS

We would like to thank National Science Foundation for the financial support under award no. 1801284 and the Department of Energy, Office Fossil Fuels, National Energy Technology Laboratory for the financial support under award no. DE-FE-0031671.

■ REFERENCES

(1) Staffell, I.; Scamman, D.; Velazquez Abad, A.; Balcombe, P.; Dodds, P. E.; Ekins, P.; Shah, N.; Ward, K. R. The role of hydrogen and fuel cells in the global energy system. *Energy Environ. Sci.* **2019**, *12*, 463−491.

(2) Hanley, E. S.; Deane, J. P.; Gallachóir, B. P. Ó. The role of hydrogen in low carbon energy futures−A review of existing perspectives. *Renewable Sustainable Energy Rev.* **2018**, *82*, 3027−3045.

(3) Hydrogen: a renewable energy perspective. *2nd Hydrog. Energy Minister. Meet.* **2019**, 5−8.

(4) Dunn, S. Hydrogen futures: toward a sustainable energy system. *Int. J. Hydrogen Energy* **2002**, *27*, 235−264.

(5) Zhu, X.; Imtiaz, Q.; Donat, F.; Müller, C. R.; Li, F. Chemical looping beyond combustion − a perspective. *Energy Environ. Sci.* **2020**, *13*, 772−804.

(6) Luo, M.; Yi, Y.; Wang, S.; Wang, Z.; Du, M.; Pan, J.; Wang, Q. Review of hydrogen production using chemical-looping technology. *Renewable Sustainable Energy Rev.* **2018**, *81*, 3186−3214.

(7) Alalwan, H. A.; Augustine, L. J.; Hudson, B. G.; Abeysinghe, J. P.; Gillan, E. G.; Mason, S. E.; Grassian, V. H.; Cwiertny, D. M. Linking Solid-State Reduction Mechanisms to Size-Dependent Reactivity of Metal Oxide Oxygen Carriers for Chemical Looping Combustion. *ACS Appl. Energy Mater.* **2021**, *4*, 1163−1172.

(8) Zhao, X.; Li, X.; Gong, Y.; Huang, K. Enhanced reversibility and durability of a solid oxide Fe−air redox battery by carbothermic reaction derived energy storage materials. *Chem. Commun.* **2014**, *50*, 623−625.

(9) Zhang, C.; Huang, K. MOF-derived iron as an active energy storage material for intermediate-temperature solid oxide iron−air redox batteries. *Chem. Commun.* **2017**, *53*, 10564−10567.
(10) Zhang, C.; Huang, K. An Intermediate-Temperature Solid Oxide Iron−Air Redox Battery Operated on O^{2-}-Chemistry and Loaded with Pd-Catalyzed Iron-Based Energy Storage Material. *ACS Energy Lett.* **2016**, *1*, 1206−1211.
(11) Xu, N.; Zhang, C.; Huang, K. Proton-mediated energy storage in intermediate-temperature solid-oxide metal−air batteries. *J. Mater. Chem. A* **2018**, *6*, 20659−20662.
(12) Zhao, X.; Li, X.; Gong, Y.; Xu, N.; Huang, K. Exploring Metal-air Chemistries with A New Solid Oxide Metal-Air Redox Battery. *ECS Trans.* **2014**, *58*, 67−74.
(13) Zhao, X.; Li, X.; Gong, Y.; Xu, N.; Huang, K. A novel intermediate-temperature all ceramic iron−air redox battery: the effect of current density and cycle duration. *RSC Adv.* **2014**, *4*, 22621−22624.
(14) Zhao, X.; Gong, Y.; Li, X.; Xu, N.; Huang, K. Cyclic Durability of a Solid Oxide Fe-Air Redox Battery Operated at 650 °C. *J. Electrochem. Soc.* **2013**, *160*, A1716−A1719.
(15) Zhao, X.; Gong, Y.; Li, X.; Xu, N.; Huang, K. A new solid oxide molybdenum−air redox battery. *J. Mater. Chem. A* **2013**, *1*, 14858−14861.
(16) Chen, S.; Zeng, L.; Tian, H.; Li, X.; Gong, J. Enhanced Lattice Oxygen Reactivity over Ni-Modified WO_3-Based Redox Catalysts for Chemical Looping Partial Oxidation of Methane. *ACS Catal.* **2017**, *7*, 3548−3559.
(17) Zeng, L.; Cheng, Z.; Fan, J. A.; Fan, L.-S.; Gong, J. Metal oxide redox chemistry for chemical looping processes. *Nat. Rev. Chem.* **2018**, *2*, 349−364.
(18) Singstock, N. R.; Bartel, C. J.; Holder, A. M.; Musgrave, C. B. High-Throughput Analysis of Materials for Chemical Looping Processes. *Adv. Energy Mater.* **2020**, *10*, 2000685.
(19) Mattisson, T.; Johansson, M.; Lyngfelt, A. The use of NiO as an oxygen carrier in chemical-looping combustion. *Fuel* **2006**, *85*, 736−747.
(20) Jiang, S.; Shen, L.; Wu, J.; Yan, J.; Song, T. The investigations of hematite-CuO oxygen carrier in chemical looping combustion. *Chem. Eng. J.* **2017**, *317*, 132−142.
(21) Adánez, J.; de Diego, L. F.; García-Labiano, F.; Gayán, P.; Abad, A.; Palacios, J. M. Selection of Oxygen Carriers for Chemical-Looping Combustion. *Energy Fuels* **2004**, *18*, 371−377.
(22) Luo, S.; Zeng, L.; Fan, L.-S. Chemical Looping Technology: Oxygen Carrier Characteristics. *Annu. Rev. Chem. Biomol. Eng.* **2015**, *6*, 53−75.
(23) Chung, C.; Qin, L.; Shah, V.; Fan, L.-S. Chemically and physically robust, commercially-viable iron-based composite oxygen carriers sustainable over 3000 redox cycles at high temperatures for chemical looping applications. *Energy Environ. Sci.* **2017**, *10*, 2318−2323.
(24) Qin, L.; Cheng, Z.; Fan, J. A.; Kopechek, D.; Xu, D.; Deshpande, N.; Fan, L.-S. Nanostructure formation mechanism and ion diffusion in iron−titanium composite materials with chemical looping redox reactions. *J. Mater. Chem. A* **2015**, *3*, 11302−11312.
(25) Ma, S.; Chen, S.; Soomro, A.; Xiang, W. Effects of CeO_2, ZrO_2, and Al_2O_3 Supports on Iron Oxygen Carrier for Chemical Looping Hydrogen Generation. *Energy Fuels* **2017**, *31*, 8001−8013.
(26) Ma, S.; Li, M.; Wang, G.; Zhang, L.; Chen, S.; Sun, Z.; Hu, J.; Zhu, M.; Xiang, W. Effects of Zr doping on Fe_2O_3/CeO_2 oxygen carrier in chemical looping hydrogen generation. *Chem. Eng. J.* **2018**, *346*, 712−725.
(27) Tian, X.; Wei, Y.; Zhao, H. Using a hierarchically-structured CuO@TiO_2-Al_2O_3 oxygen carrier for chemical looping air separation in a paralleled fluidized bed reactor. *Chem. Eng. J.* **2018**, *334*, 611−618.
(28) Karimi, E.; Forutan, H. R.; Saidi, M.; Rahimpour, M. R.; Shariati, A. Experimental Study of Chemical-Looping Reforming in a Fixed-Bed Reactor: Performance Investigation of Different Oxygen Carriers on Al_2O_3 and TiO_2 Support. *Energy Fuels* **2014**, *28*, 2811−2820.
(29) Liu, Y.; Qin, L.; Cheng, Z.; Goetze, J. W.; Kong, F.; Fan, J. A.; Fan, L.-S. Near 100% CO selectivity in nanoscaled iron-based oxygen carriers for chemical looping methane partial oxidation. *Nat. Commun.* **2019**, *10*, 5503.
(30) Garai, M. H. S.; Khosravi-Nikou, M. R.; Shariati, A. Chemical Looping Steam Methane Reforming via Ni-ferrite Supported on Cerium and Zirconium Oxides. *Chem. Eng. Technol.* **2020**, *43*, 1813−1822.
(31) Jin, X.; Zhao, X.; Huang, K. A high-fidelity multiphysics model for the new solid oxide iron-air redox battery part I: Bridging mass transport and charge transfer with redox cycle kinetics. *J. Power Sources* **2015**, *280*, 195−204.
(32) Piotrowski, K.; Mondal, K.; Wiltowski, T.; Dydo, P.; Rizeg, G. Topochemical approach of kinetics of the reduction of hematite to wüstite. *Chem. Eng. J.* **2007**, *131*, 73−82.
(33) Monazam, E. R.; Breault, R. W.; Siriwardane, R. Kinetics of Hematite to Wüstite by Hydrogen for Chemical Looping Combustion. *Energy Fuels* **2014**, *28*, 5406−5414.
(34) Dang, J.; Chou, K.-C.; Hu, X.-J.; Zhang, G.-H. Reduction Kinetics of Metal Oxides by Hydrogen. *Steel Res. Int.* **2013**, *84*, 526−533.
(35) Barde, A. A.; Klausner, J. F.; Mei, R. Solid state reaction kinetics of iron oxide reduction using hydrogen as a reducing agent. *Int. J. Hydrogen Energy* **2016**, *41*, 10103−10119.
(36) Spreitzer, D.; Schenk, J. Reduction of Iron Oxides with Hydrogen—A Review. *Steel Res. Int.* **2019**, *90*, 1900108.
(37) Janković, B.; Adnađević, B.; Jovanović, J. Application of model-fitting and model-free kinetics to the study of non-isothermal dehydration of equilibrium swollen poly (acrylic acid) hydrogel: Thermogravimetric analysis. *Thermochim. Acta* **2007**, *452*, 106−115.
(38) Ma, Z.; Zhang, S.; Xiao, R.; Wang, J. Inhibited Phase Segregation to Enhance the Redox Performance of $NiFe_2O_4$ via CeO_2 Modification in the Chemical Looping Process. *Energy Fuels* **2020**, *34*, 6178−6185.
(39) Zhu, X.; Wei, Y.; Wang, H.; Li, K. Ce−Fe oxygen carriers for chemical-looping steam methane reforming. *Int. J. Hydrogen Energy* **2013**, *38*, 4492−4501.
(40) Zhang, C.; Ji, C.; Wang, W.; Schmidt, D.; Jin, X.; Lemmon, J. P.; Huang, K. A dynamic solid oxide fuel cell empowered by the built-in iron-bed solid fuel. *Energy Environ. Sci.* **2016**, *9*, 3746−3753.
(41) Wilke, S. K.; Dunand, D. C. Fe−Ni foams self-heal during redox cycling *via* reversible formation/homogenization of a ductile Ni scaffold. *J. Mater. Chem. A* **2020**, *8*, 19375−19386.

https://doi.org/10.1021/acsaem.1c01152
ACS Appl. Energy Mater. XXXX, XXX, XXX−XXX